

Boosting the Performance of Pt/C Catalysts via Nitrogen-Doped Carbon Support: Insights from Structural and Electrochemical Characterization

Yulia A. Bayan, Egor R. Beskopylny, Evgeny U. Gerasimov, Egor E. Aydakov, Kirill K. Volik, Ilya V. Pankov, Ilya V. Chepkasov, Michael M. Lukyanov, Alexander G. Kvashnin, and Anastasia A. Alekseenko*

Nitrogen-doped carbon supports enhance platinum electrocatalysts for proton exchange membrane fuel cells (PEMFCs). This study demonstrates a rapid melamine-assisted N-doping method for conductive carbon black (Ketjenblack EC600JD), producing a high-loading (≈ 40 wt.% Pt) catalyst with exceptional activity and durability. X-ray photoelectron spectroscopy confirms successful N-incorporation. Microscopy reveals uniform Pt nanoparticles (2.5–3 nm) and atomic Pt clusters on the N-doped support, attributed to strong Pt–N interactions. Density functional theory (DFT) calculations highlight the critical role of pyridinic-N defects in stabilizing atomic Pt, enhancing activity via charge transfer, and improving stability via strong Pt anchoring. Electrochemically, Pt/KB-600-N achieves twice the mass activity of commercial HiSPEC4000. After accelerated stress testing, it shows only a 15% electrochemical surface area (ESA) loss versus 35% for undoped Pt/KB-600. Enhanced stability correlates with pyridinic/graphitic N species mitigating carbon corrosion and Pt detachment. Binding energy analysis and cluster models quantify the Pt-support interaction, revealing N-doping increases Pt adhesion energy by 20–30% compared to pristine carbon. This work establishes a rational design strategy for high-performance Pt-based electrocatalysts by leveraging nitrogen-doped carbon supports, offering fundamental insights into the critical role of Pt–N interactions in enhancing both activity and durability for PEMFC applications.

1. Introduction

Platinum-based electrocatalysts play a pivotal role in proton exchange membrane fuel cells (PEMFCs), remaining the dominant component for both cathode and anode processes in the

catalyst market.^[1,2] The exceptional catalytic performance of platinum in the oxygen reduction reaction (ORR) and hydrogen oxidation reaction makes it essential for the efficient functioning of fuel cells.^[3–5] However, the high cost of Pt and limited natural abundance have driven extensive research efforts to reduce its loading in catalysts while simultaneously enhancing their activity and durability.^[6] While significant progress has been made in understanding and improving conventional Pt/C catalysts, a critical challenge persists in achieving high Pt dispersion and stability at industrially relevant high metal loadings (>30 wt.%), which are essential for maximizing power density in practical applications.^[7–9]

The modification of carbon supports used as conductive substrates for platinum nanoparticle dispersion have been widely recognized as a key strategy for improving the performance of nanostructured catalysts.^[10] Carbon materials such as carbon black, nanotubes, and graphene, and their derivatives, exhibit high specific surface area, electrical conductivity, and chemical stability, which makes them ideal supports for catalytically active platinum nanoparticles.^[9–12] Commercial carbon blacks including Vulcan XC-72, Ketjenblack EC-300J, and KetjenBlack EC600JD are widely used as a support for platinum–carbon catalyst

Y. A. Bayan, E. R. Beskopylny, A. A. Alekseenko
Southern Federal University
Faculty of Chemistry
7 Zorge St., Rostov-on-Don 344090, Russia
E-mail: aalekseenko@sfedu.ru

E. U. Gerasimov, E. E. Aydakov
Department of Catalysis Research
Boreskov Institute of Catalysis
Prospect Ac. Lavrentieva 5, Novosibirsk 630090, Russia

K. K. Volik
Southern Federal University
The Smart Materials Research Institute
178/24 Andrey Sladkova St., Rostov-on-Don 344090, Russia

I. V. Pankov
Southern Federal University
Research Institute of Physical Organic Chemistry
194/2 St., Rostov-on-Don 344090, Russia
I. V. Chepkasov, M. M. Lukyanov, A. G. Kvashnin
Skolkovo Institute of Science and Technology
Bolshoy Boulevard 30, bld. 1, Moscow 121205, Russia
I. V. Chepkasov
Katanov Khakas State University
90 Lenin pr., Abakan 655017, Russia

 The ORCID identification number(s) for the author(s) of this article can be found under <https://doi.org/10.1002/smll.202510144>

DOI: 10.1002/smll.202510144

synthesis in fuel cell applications.^[10,13,14] These supports demonstrate significant differences in their microstructural characteristics, specifically in terms of specific surface area and micro/mesopore content. These factors critically influence the dispersion of platinum nanoparticles and, consequently, determine the electrochemical performance of Pt/C catalysts. The most thoroughly studied and industrially adopted support is Vulcan XC-72, offering an optimal balance between cost, availability, and functional properties with a specific surface area of $\approx 260 \text{ m}^2 \text{ g}^{-1}$.^[15] However, KetjenBlack carbon materials with their higher specific surface area ($> 700 \text{ m}^2 \text{ g}^{-1}$) and greater micro/mesopore content may be more suitable for preparing Pt/C catalysts with metal loadings exceeding 30 wt.%, enabling superior nanoparticle distribution.^[13]

It has been well established that improving the performance of Pt-based catalysts performance requires targeted modification of the carbon supports.^[10,16–18] Common chemical modification approaches include surface oxidation,^[19] functionalization with various groups^[20] (e.g., carboxyl, hydroxyl, or amino groups), and heteroatom doping (nitrogen, boron, phosphorus, etc.).^[16,18,21–23] Nitrogen doping of carbon black has been shown to be a promising technique, as it can lead to a more uniform distribution of metal nanoparticles and improve their adhesion to the surface.^[14,24,25] This can enhance the electrochemical properties of electrocatalysts. The effectiveness of nitrogen-doped carbon supports has been further confirmed in recent studies,^[14,24,26,27] indicating that nitrogen anchored on the carbon support surface plays a crucial role in platinum nanoparticle stabilization.^[28,29] Pyridinic and pyrrolic nitrogen atoms located at the edges or defects of the carbon structure are particularly effective in enhancing Pt-support interactions.^[28,29] The lone electron pairs in these nitrogen groups can interact with platinum atoms, strengthening the adhesion between them and preventing the nanoparticles from agglomerating or detaching. The beneficial effect of graphitic nitrogen on the electrochemical performance of platinum-based materials has been demonstrated by Stambula et al.^[30] Tachibana et al.^[14,31] developed a nitrogen-doped carbon black through multistep processing, including treatment with a nitrogen-containing cyanamide precursor. Their studies showed that N-doped supports have intrinsic electrocatalytic activity for the ORR and can serve as effective substrates for the preparation of catalysts with uniformly distributed platinum nanoparticles.^[14,31] Notably, conventional N-doped carbon synthesis methods usually involve multiple steps that take anywhere from 6 to 24 h.^[14,32–36] Recent works by the P. Strasser group have demonstrated the feasibility of modifying the Ketjenblack EC-300J carbon support via a process with a total duration of $\approx 20 \text{ h}$ to produce model catalysts with a platinum loading of up to 20 wt.% and promising performance in membrane electrode assemblies (MEAs).^[37,38] This significant research activity in the field reflects both the high relevance of the topic and the ongoing debates within the scientific community.

In this study, we propose the development of a rapid support modification approach that minimizes time and resource expenditure. Most fundamental studies focus on synthesizing and investigating model 20% Pt/C catalysts, but these systems do not always exhibit the same property correlations when transitioning to higher metal loadings. Our modified support is designed to ensure superior platinum nanoparticle distribution when prepar-

ing Pt/C catalysts with $\approx 40\%$ metal loading. Moreover, we perform a systematic analysis of the relationship between N-doping of porous carbon, catalytic activity and degradation resistance of Pt-based materials. The improvements of Pt dispersion and higher mass activity on N-doped carbon are investigated by density functional simulations of the migration of Pt atoms and Pt nanoparticles on graphene. The synthesis of high-performance 40% Pt/C electrocatalysts for PEMFC applications based on KetjenBlack EC600JD and its derivatives is confirmed.

Although MEAs provide a more accurate representation of real fuel cell operating conditions, the rotating disk electrode (RDE) method continues to be the preferred choice for early-stage catalyst development. This approach is essential for fundamental catalyst evaluation, as it allows for more efficient testing (requiring over 10 times less catalyst material than MEA testing) and reduces system complexity, while providing superior control over experimental parameters. In our investigation, we modify Pt/C electrocatalysts and evaluate their activity and stability using the RDE approach. This allows us to perform a detailed analysis of key performance characteristics prior to full-scale testing with MEA.

The novelty and cutting-edge contributions of the present work are threefold: i) A rapid and scalable strategy for support modification to incorporate nitrogen species, offering a significant time and energy advantage over conventional prolonged processes; ii) The development of highly-dispersed catalysts (2.5–3 nm for $\approx 80\%$ of nanoparticles) with an ultra-high platinum loading of $\approx 40 \text{ wt.}\%$; iii) A comprehensive investigation of the structure–activity–stability relationship through a combined experimental and DFT theoretical analysis, linking the enhanced electrochemical performance to the presence of pyridinic-N defects.

2. Results and Discussion

2.1. Characterization of Carbon Supports and Catalysts

The modification of the Ketjenblack EC600JD carbon support with a nitrogen-containing compound is carried out in a tube furnace. The nitrogen adsorption and desorption isotherms at 77 K for two carbon materials, KB-600 and KB-600-N are shown in Figure 1a,b. Isotherms are analyzed using the Brunauer–Emmett–Teller (BET) method, a widely used technique for determining the specific surface area and pore characteristics of porous materials. Both KB-600 and KB-600-N exhibit Type IV isotherms, which are characteristic of mesoporous materials with a significant increase in nitrogen adsorption at high relative pressures. This behavior is directly related to capillary condensation – a phenomenon in which a gas condenses into a liquid-like state within pores at pressures below the saturation vapor pressure (P_0). As seen from the isotherms (Figure 1a,b), both supports, KB-600 and KB-600-N, display a sharp rise in nitrogen adsorption as P/P_0 approaches 1, while the Pt/KB-600-N catalyst demonstrates a significantly higher adsorption capacity of up to 1300 mmol g^{-1} compared to 100 mmol g^{-1} for the pristine supports. This substantial increase is attributed to monolayer adsorption on pore walls at low relative pressures ($P/P_0 < 0.3$), while capillary condensation in mesopores begins at $P/P_0 > 0.7$, as described by the Kelvin equation.^[39] The hysteresis between the adsorption and desorption branches (Figure 1a) further confirms

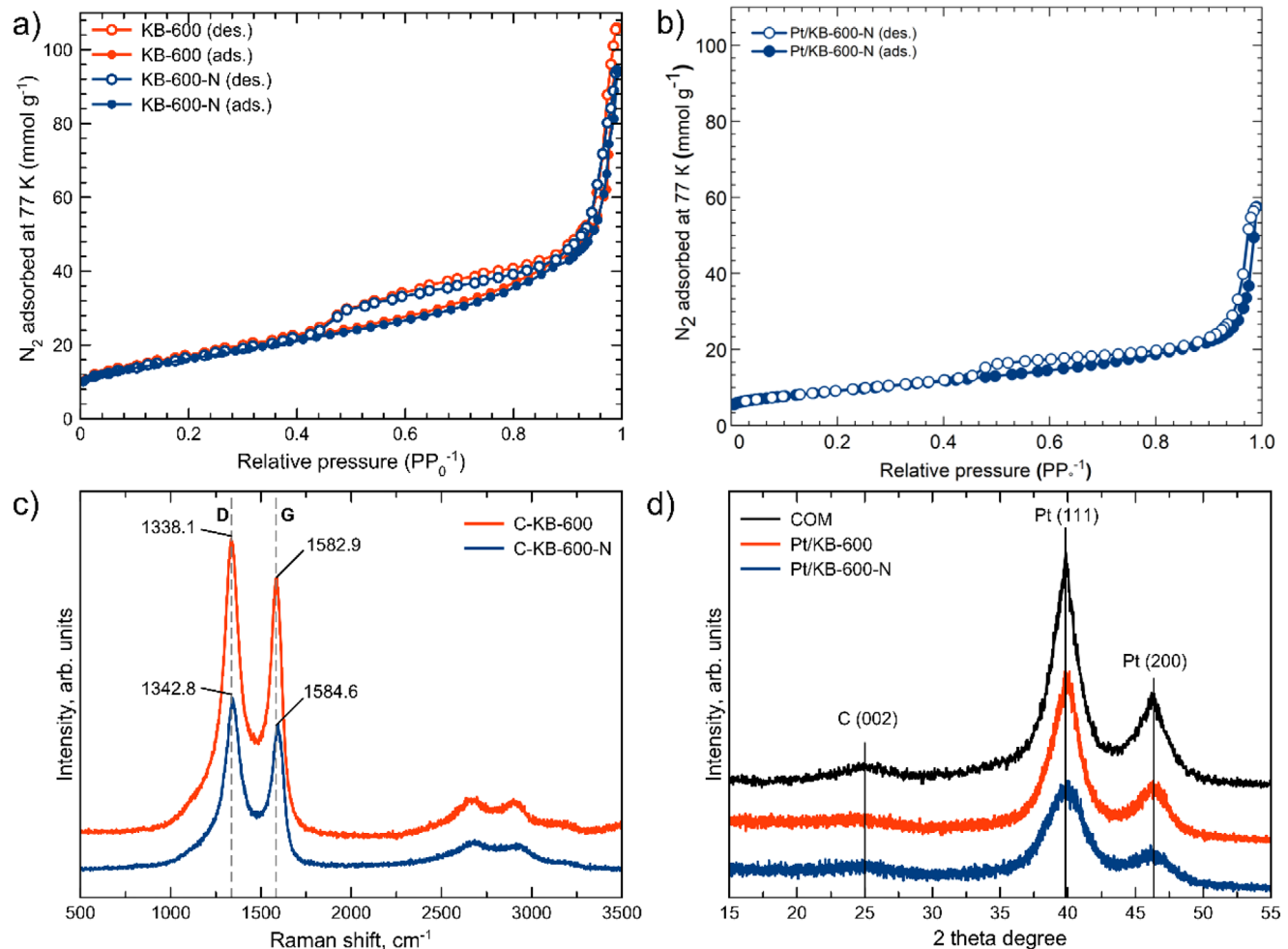


Figure 1. Nitrogen adsorption isotherms for a) KB-600 and KB-600-N supports and b) Pt/KB-600-N electrocatalyst. c) Raman spectra for the KB-600 and KB-600-N carbon supports. d) XRD patterns of the Pt/KB-600, Pt/KB-600-N and COM catalysts.

the presence of mesopores, where capillary condensation occurs at different P/P_0 values during adsorption and desorption.

The dV/dD distribution shows the predominance of micropores with maxima in the pore width range of ≈ 0.7 nm. This distribution also reveals the presence of mesopores with widths between 2 and 3 nm (Figure S2, Supporting Information). According to the BET analysis of KB-600 and KB-600-N carbon supports, there is no significant difference in specific surface area between pristine and modified carbon supports, see Figure 1a. Detailed information is presented in Table S1 (Supporting Information).

Figure 1c presents the Raman spectra of the KB-600 and KB-600-N supports. The spectra exhibit two intense peaks located at ≈ 1340 and ≈ 1585 cm⁻¹, referred to as the D-band and G-band, respectively. These wavenumbers correspond to carbon with sp³-hybridized bonds. These peaks provide information about the structural and electronic properties of the materials. The D peak corresponds to disorder and defects in the carbon structure, typically associated with sp³-hybridized carbon atoms or edges of graphene layers. The G peak represents the graphitic structure of sp²-hybridized carbon atoms, indicative of ordered graphitic domains. This rise in the I_D/I_G ratio provides direct evidence of

the enhanced defect density in the structure of the modified support, which is the primary structural effect expected from successful nitrogen doping.^[40–43] Minor shifts in the positions of the D and G bands were also noted but were not used as the primary evidence for doping or disorder (Figure 1c).

The X-ray diffraction (XRD) patterns of the Pt/KB-600, Pt/KB-600-N, and commercial COM catalysts are presented in Figure 1d. All samples exhibit characteristic peaks of the face-centered cubic crystal structure of platinum, with the most intense reflections corresponding to the (111) and (200) planes at 2 θ values of $\approx 39.8^\circ$ and 46.3° , respectively. A broad peak at $\approx 25^\circ$ is attributed to the (002) plane of the graphitic carbon support, confirming its disordered structure. Notably, the Pt/KB-600-N sample exhibits the broadest reflection peak for the Pt (111) plane, indicative of smaller platinum crystallites compared to Pt/KB-600 and COM, as corroborated by Scherrer analysis (Table S2, Supporting Information). The reduced crystallite size in Pt/KB-600-N suggests that nitrogen doping of the Ketjenblack EC-600JD support enhances Pt dispersion.

The obtained Pt/C electrocatalysts based on different carbon supports are characterized by a platinum mass fraction close to

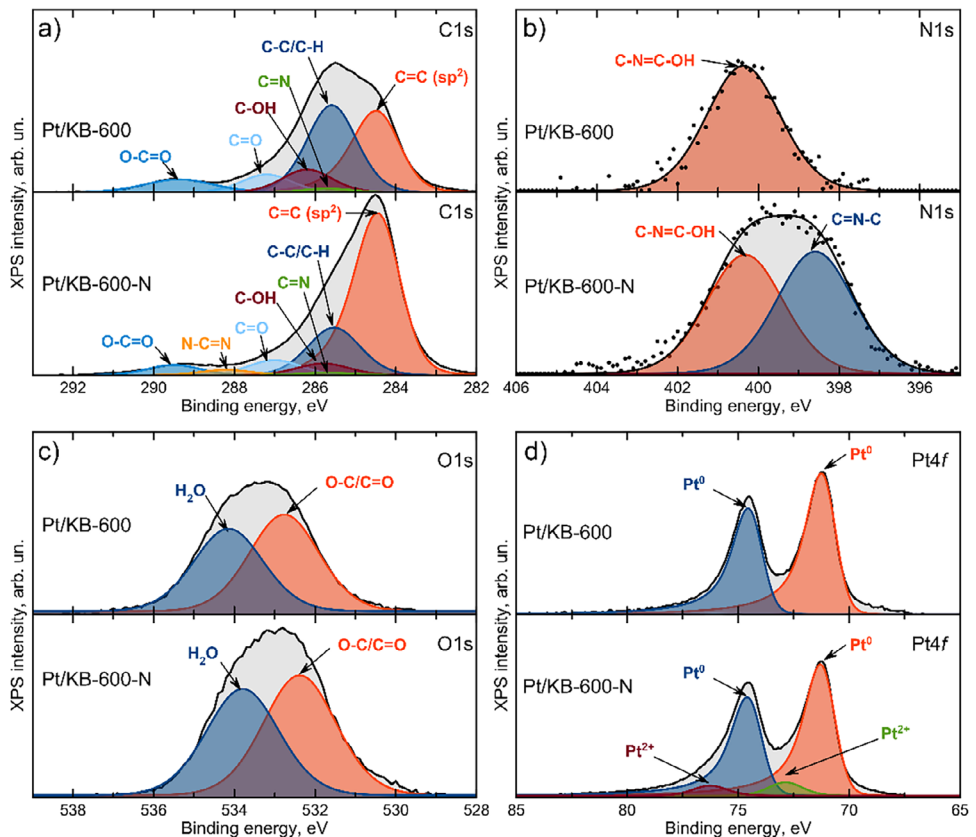


Figure 2. XPS analysis of synthesized samples. Measured spectra of a) C1s, b) N1s, c) O1s, and d) Pt4f core-level spectra of the Pt/KB-600 and Pt/KB-600-N catalysts. The spectra are normalized to the total intensity of the corresponding C1s spectra.

40%, enabling their further comparison with the commercial HiSPEC4000 sample (Table S2, Supporting Information). The surface area, determined by the BET method for the Pt/KB-600-N sample, is expectedly reduced due to the deposition of platinum nanoparticles on the support surface and partial blocking of micropores (Figure 1b; Table S1, Supporting Information).

The successful doping of the carbon support with nitrogen is confirmed by the X-ray photoelectron spectroscopy (XPS) results for the catalysts Pt/KB-600 and Pt/KB-600-N. These catalysts are based on the pristine and nitrogen-modified support, respectively. Reflections corresponding to C, O, N, and Pt are detected in the core-level spectra of the samples, see Figure 2. Table S3 (Supporting Information) presents the atomic ratios of elements in the near-surface layer of the samples.

In the Pt/KB-600 catalyst, the nitrogen content is negligible, with an atomic ratio of $[N]/[C] = 0.005$. These trace amounts of nitrogen may have been present in the carbon support in its initial state. The Pt/KB-600-N electrocatalyst, based on the modified KB-600-N support, has a $[N]/[C]$ ratio of 0.017, which is four times higher than that of Pt/KB-600, as shown in Table S3 (Supporting Information).

Figure 2a shows the C1s spectra of the Pt/KB-600 and Pt/KB-600-N samples. The C1s spectra are composed of several peaks, which correspond to carbon in chemical environments. Based on the refs. [44–47], these peaks, namely can be attributed to C=C/C–H (285.5 eV), C=N (285.7 eV), C–OH (286.2 eV), C=O

(287.2 eV), N=C=N (288.2 eV), and O=C=O (289.4 eV) bonds. The increase in the C=C peak intensity is attributed to the pyrolysis of the support during thermal treatment. While this thermal process alters the carbon bonding environment, our previous work^[48] demonstrated that it does not adversely affect the electrochemical corrosion resistance of the support. On the contrary, the decisive factor for the enhanced stability is the concomitant nitrogen doping, which is corroborated by the superior performance of the KB-600-N material in accelerated stress tests (see Section 3.3, Supporting Information). The N1s spectrum of Pt/KB-600 (see Figure 2b) shows a single peak at 400.4 eV, which can be attributed to the pyridinic C=N=C–OH groups.^[49] The N1s spectrum of Pt/KB-600-N sample (Figure 2b) shows two peaks at 398.6 and 400.4 eV. The extra peak corresponds to the pyridinic C=N=C groups. This suggests that doping with nitrogen leads to the appearance of new C=N=C species on the KB-600-N support. We cannot rule out the presence of a minor fraction of pyrrolic nitrogen, whose signals may be present in the XPS spectrum depending on the specific fitting procedure.^[50,51]

The O1s spectra of the investigated samples are well described by two peaks with binding energies ≈ 532.4 – 532.7 and 533.8 – 534.1 eV (Figure 2c). The first peak is characteristic of oxygen forming bonds with carbon, mainly. The second peak can be attributed to oxygen from adsorbed water molecules^[44,47] (see Figure 2c; Table S4, Supporting Information).

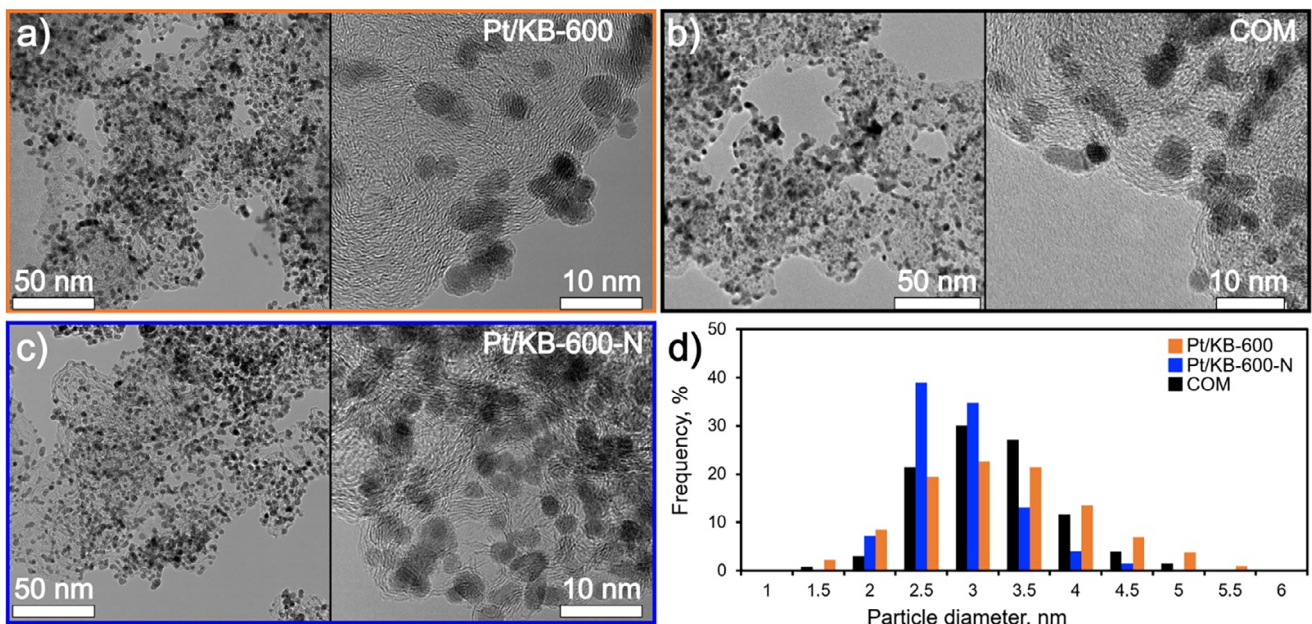


Figure 3. TEM micrographs of the Pt/C catalysts. a) Pt/KB-600, b) COM, c) Pt/KB-600-N. d) Size distribution histogram of the Pt nanoparticles on the considered samples.

The Pt4f spectrum shows a doublet of $\text{Pt}4\text{f}_{7/2}$ – $\text{Pt}4\text{f}_{5/2}$ (see Figure 2d) with a spin-orbit splitting of 3.33 eV. The $\text{Pt}4\text{f}_{7/2}$ binding energy of bulk metallic platinum is reported to be 71.1–71.6 eV^[52] (Table S4, Supporting Information). For the Pt/KB-600 sample, the Pt4f spectrum is well approximated by a single spin-orbital doublet $\text{Pt}4\text{f}_{7/2}$ – $\text{Pt}4\text{f}_{5/2}$ with the $\text{Pt}4\text{f}_{7/2}$ binding energy ≈71.1 eV, corresponding to platinum in the metallic state. The absence of higher oxidation state components indicates that platinum predominantly exists in its reduced form on the undoped Ketjenblack support, consistent with the weak metal–support interaction expected for pristine carbon materials. The symmetric line shape and narrow full width at half maximum of the Pt4f peaks suggest a homogeneous electronic environment for the Pt nanoparticles in this catalyst.

In contrast, the Pt4f spectrum of the nitrogen-doped Pt/KB-600-N catalyst reveals a more complex electronic structure. In addition to the metallic Pt^0 doublet at 71.1 eV, a second doublet appears at higher binding energy at 72.8 eV, which can be assigned to oxidized platinum species in the oxidation Pt^{2+} state (Table S4, Supporting Information). We propose that platinum atoms and clusters in an oxidized state are localized at the sites of N-functional groups, as indicated by X-ray spectroscopy (EDX) line-scanning (Figure S3, Supporting Information).

Obtained characterization of the samples by XRD, Raman spectroscopy, and accounting for surface chemical composition features determined by XPS, the distinct differences between the catalysts based on modified and pristine supports are observed. These structural variations are expected to influence their electrochemical behavior.

To analyze the distribution of platinum nanoparticles on the surface of carbon supports in the catalysts, transmission electron microscopy studies are conducted. TEM images of all samples reveal the presence of microspheres densely covered by plat-

atinum nanoparticles, as shown in Figure 3. Figure 3a shows the TEM images of the Pt/KB-600 sample. The significant number of metallic nanoparticles distributed across the substrate is a result of working with the materials used in PEMFCs that have a platinum loading of ≈40%, rather than with model systems featuring low PGM loading. Nanoparticle agglomeration is common in all materials, including Pt/KB-600 and COM, but in the catalyst based on nitrogen-modified carbon it is minimized, as seen in Figure 3a,b. The TEM images of the local areas of this sample show a more uniform spatial distribution of nanoparticles on the substrate (Figure 3c).

Considering the size of Pt nanoparticles one should note that the COM sample exhibits a broad size distribution of platinum nanoparticles, ranging from 1.5 to 5.5 nm (Figure 3d). This significant heterogeneity in nanoparticle size may be attributed to the synthesis method or production conditions of the benchmark catalyst. For the Pt/KB-600 sample, a narrower size distribution is observed (see orange bars in Figure 3d) with more than 70% of nanoparticles falling within the range 2.5–3.5 nm on the Pt/KB-600 support. In the case of the Pt/KB-600-N sample, synthesized using the modified support, the distribution becomes even narrower, see blue bars in Figure 3d. In this case, more than 70% of the platinum nanoparticles have a size of 2.5–3 nm, expecting better electrochemical behavior of the electrocatalyst.

A comprehensive investigation of the structural features of Pt nanoparticles is then performed using HAADF-STEM analysis. Microscopy images of localized areas in the Pt/KB-600 and Pt/KB-600-N samples show atomic layers of nanoparticles, along with high surface crystallinity (Figure 4a,b). The HAADF-STEM images of the Pt/KB-600-N reveal the presence of clusters and individual platinum atoms (Figure 4b). The existence of platinum clusters on the surface of nitrogen-doped carbon supports

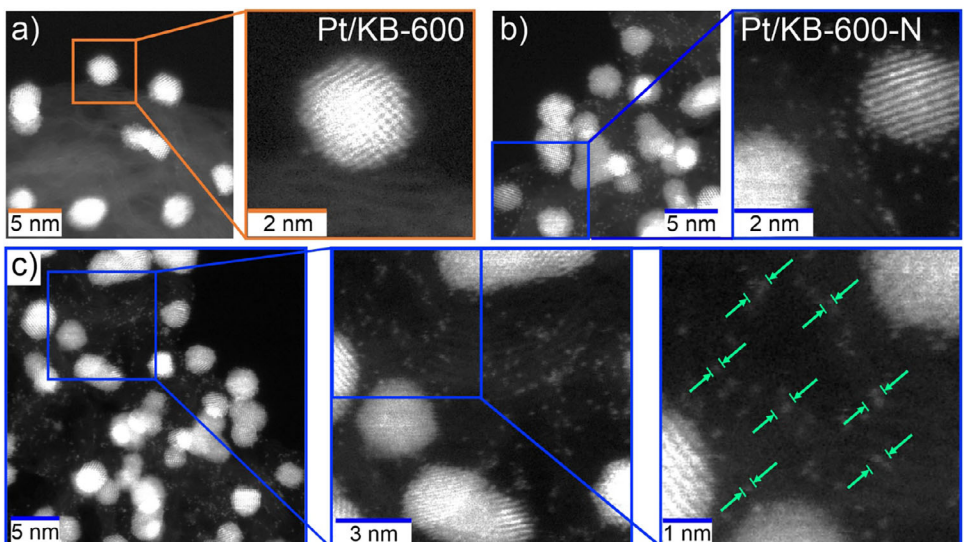


Figure 4. HAADF-STEM images of a) Pt/KB-600, b) Pt/KB-600-N. c) HAADF-STEM images of different regions of the Pt/KB-600-N sample. Arrows indicate the location of small individual platinum clusters.

has been demonstrated previously for N-doped Ketjenblack EC-300.^[48]

Additionally, EDX mapping (Figure S3, Supporting Information) reveals a uniform spatial distribution of nitrogen throughout the carbon substrate. This suggests that the doping process was effective not only on the surface but also throughout the bulk volume of the porous support structure. Besides we perform EDX line scanning of localized areas of the surface of the Pt/KB-600-N sample, see Figure S4 (Supporting Information). The increase in the intensity of the nitrogen signal is observed at the same places where platinum nanoparticles are located (Figure S4, Supporting Information).

To understand the enhanced dispersion of Pt nanoparticles and their higher mass activity on nitrogen-doped carbon supports, a DFT simulation of the migration of a Pt atom and a nanoparticle on graphene is performed, together with calculations of migration barriers and charge transfer.

2.2. Density Functional Calculations

For computational analysis, the graphene structure is used as a model for amorphous carbon support in experiments. Real amorphous carbons are structurally complex and heterogeneous, consisting of a disordered network of hybridized sp^2 (graphite-like) and sp^3 (diamond-like) carbon atoms. Most amorphous catalysts used as supports are predominantly sp^2 -hybridized, so studying catalysts on graphene essentially studies the interaction with this common structural motif. Using graphene as a support model, we can create different types of defects in the graphene sheet to study. Given the scale of the defects and the size of the nanoparticles, one can note that the local area where the most significant and crucial interaction between the support and catalyst occurred can be approximated by a flat surface.

These insights gained from graphene simulations provide a foundational understanding that can be used to interpret com-

plex experimental data on real amorphous carbon systems and to guide the rational design of better catalysts. It should also be pointed out that amorphous carbon is often a porous 3D material, while graphene is a 2D sheet. Moreover, structural imperfections such as edges (which can also be functionalized) may also appear in amorphous carbons. Thus, the model of graphene used as a support does not consider the effect caused by the curvature or edges of graphene on the catalyst or its properties.

Several graphene defects, including graphitic-N and pyridinic-N types are considered (the latter involving a carbon monovacancy containing a nitrogen atom;^[53] see Figure S5, Supporting Information). The presence of nitrogen atoms leads to the distortion of the graphene structure and the charge redistribution, compared to pure graphene. Nitrogen defect acts as an acceptor of electrons (the nitrogen atoms pull $\approx 1.2 e^-$) and a pronounced redistribution is observed in the electron localization function, as shown in Figure S5 (Supporting Information).

The results of the simulation of the migration of the Pt atom and the Pt_{38} nanoparticle on pure graphene surface with graphitic N-type defects together with energy barriers are presented in the Figures S6–S11 (Supporting Information). The most interesting situation may occur during the interaction between Pt (atom or nanoparticle) with pyridinic-N defects, which are common for graphene.^[2] These defects contain a carbon monovacancy with a nitrogen atom, see Figure 5a,b. Three types of pyridinic-N defects are considered to explore the role of nitrogen in the migration of Pt on the graphene. Migration pathways only through the vacancy are considered as shown in Figure 5a,b. Calculated energy barriers are shown in Figure 5c,d. It is clearly seen that the pyridinic-N defect plays the role of a trap for the Pt atom (Figure 5c). There is an energy well instead of an energy barrier. The depth of the well depends on the number of nitrogen atoms in the pyridinic defect. One can see that the presence of one nitrogen atom (MV-1N type) leads to the depth energy well of ≈ 4.32 eV, while for two nitrogen atoms the depth of the well decreases to 2.75 eV. Fully saturated carbon monovacancy by nitrogen atoms (MV-3N) leads

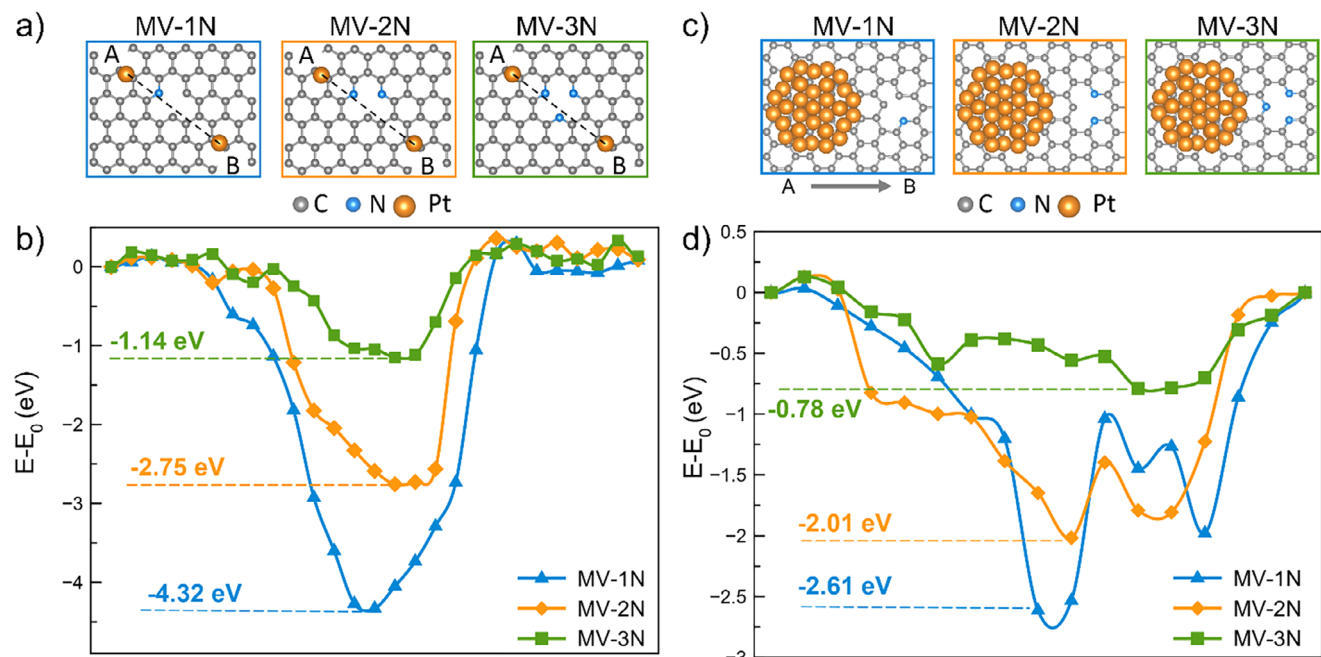


Figure 5. General scheme of migration pathways considered for a) Pt atom and b) Pt₃₈ nanoparticle along the surface of graphene with pyridinic-N defects. Calculated energy barriers of the migration of c) Pt atom and d) Pt₃₈ nanoparticle.

to the lowest depth of the energy well of 1.14 eV. This data allows us to make a conclusion about the role of nitrogen in the trapping of Pt atoms. More nitrogen atoms in the pyridinic defects observed, a lower energy barrier is for the migration of the Pt atom from the well to graphene.

A similar situation is observed for the case of migration of Pt₃₈ nanoparticle, see Figure 5d. Pyridinic-N defects influence much pronounced compared to graphitic-N, see Figure S6 (Supporting Information). For the nanoparticle, the depth of the energy well decreases as the number of nitrogen atoms in the pyridinic defect increases. One can see that here the difference in the energy wells is not so high as for the atom which is related to the relative sizes of the pyridinic-N defect and nanoparticle. Thus, based on all the provided information we can conclude that pyridinic-N defects in graphene may serve as traps for Pt nanoparticles. This trapping effect is directly corroborated by our experimental observations, where small Pt nanoparticles and individual atoms remain fixed at their original positions on the graphene support without segregating into larger particles.

As energetically, it is more favorable for the Pt atom to be fixed on pyridinic-N defects. We study how the effect of trapping by nitrogen defects influences the adsorption of an oxygen molecule on platinum. Calculation of Bader's charges showed that electrons flow from the platinum atom to the oxygen molecule (Figure 6). The amount of this charge varies greatly depending on the type of defect in graphene. The largest charge transfer from Pt to the oxygen molecule (0.9 electrons) is observed in pyridinic-N defects containing a carbon monovacancy with two nitrogen atoms (see MV-2N in Figure 6d). In order to understand how the additional charge on the oxygen molecule affects the oxygen–oxygen bond, Crystal Orbital Hamilton Populations (COHPs) and integrated COHP (ICOHP) calculations are per-

formed. Details about COHP analysis can be found in the Supporting Information. Calculated –COHP diagrams are shown in Figure 6f-k. In the case of MV-2N, when the maximum amount of charge flows onto the oxygen molecule, we see the greatest weakening of the oxygen–oxygen bond with ICOHP = -4.16 eV for both spin up and down which is more than in other cases. An increase in the O–O bonding distance to 1.46 Å is also observed (Figure 6i), and thus we expect the oxygen dissociation barrier to be lower in the case of MV-2N defect than in any other cases involving a platinum atom on graphene.

Consideration of Pt₃₈ nanoparticles allows us to determine the role of size in the trapping effect observed in experiments. The charge transfer to oxygen molecules adsorbed on a Pt₃₈ nanoparticle located on graphene with N-type defects is calculated. It is found that the charge transfer from Pt₃₈ to O₂ is spatially heterogeneous, with molecules closest to the graphene-Pt interface receiving more charge than others. This indicates that the most catalytically active region of a nanoparticle is likely to be at the interface between the particle and support, where maximum charge redistribution facilitates electron donation to adsorbed O₂. Similar to the case of a single Pt atom, the amount of charge transferred depends on the specific type of graphene defect. Figure 7f-h shows the average charge transfer, ICOHP of O–O bonds and O–O distance in O₂ molecules adsorbed onto the first, second, and third layers of Pt₃₈ depending on the type of graphene defect. The data clearly reveal distinct behavior for the first layer (1L) of O₂ compared to the 2L and 3L. As in the case of a single Pt atom, the MV-2N defect leads to the greatest charge transfer to oxygen in the first layer (1L).

The comparison between the adsorption characteristics of a single atom and a nanoparticle can be made by calculating the charge excess, bond strength (ICOHP), and the O–O bonding

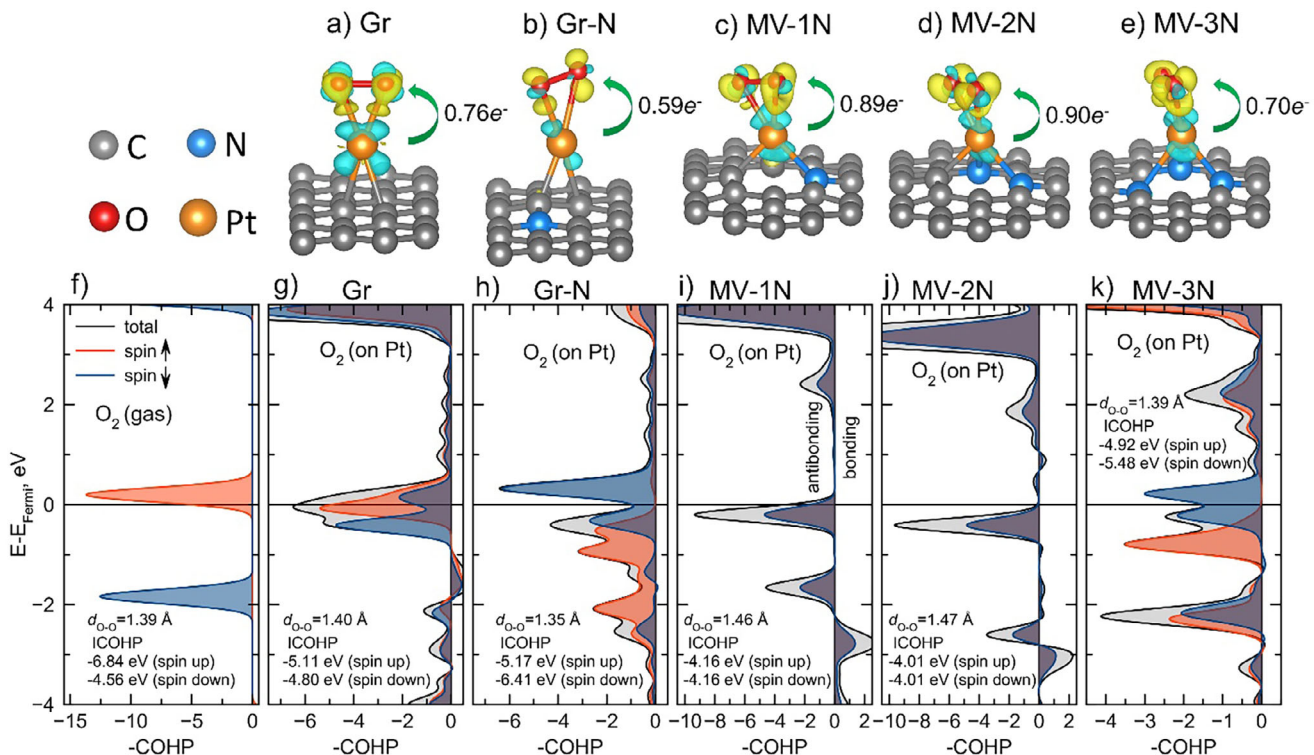


Figure 6. Visualized Bader's charge redistribution for O_2 molecules adsorbed on Pt atoms on a) graphene, b) graphene with graphitic-N defect, c–e) graphene with pyridinic-N defects with 1, 2, and 3 nitrogen atoms (MV-1N, MV-2N, and MV-3N respectively). The yellow color of the density corresponds to an excess of electrons, whereas the blue color corresponds to an electron deficiency. The isosurface value for charge density is $0.1 \text{ e } \text{\AA}^{-3}$. f–k) Calculated integrated COHP (ICOHP) diagrams which reflect the bond strength (the more negative value, the stronger the bond strength) for all studied systems.

distance in O_2 as a function of the defect type of graphene, see Figure 8. In the case of a nanoparticle, these are calculated for only the first layer (1L). Clearly, in the case of one platinum atom, the oxygen molecule has the highest excess charge, see Figure 8a. This excess charge weakens the bond and increases the O–O distance, facilitating easier dissociation of oxygen during the ORR. Graphitic-N defects are least effective at transferring charge from Pt_{38} to O_2 , according to data from Figure 8b. The more electrons are transferred, the more occupied are the antibonding orbitals (Figure 8b), making it easier to activate O_2 .^[54] Thus, our calculations show that pyridinic-N defects are more active in the ORR than graphitic-N. This is also confirmed experimentally.

2.3. Electrochemical Performance

The electrochemical behavior of carbon supports under stress testing conditions is studied using the rotating disk electrode method with two distinct protocols: 1.4 and 0.8 V for 36 cycles and 1–1.5 V for 5000 cycles. Details can be found in Section 6.2 (Supporting Information), where the initial cyclic voltammograms of the KB-600 and KB-600-N supports are shown in Figures S12 and S13 (Supporting Information). The doped electrodes do not show any characteristic pseudocapacitive peaks in the range of 0.5–0.7 V, which are typically associated with oxygen-containing functional groups on the surface. Post-testing characterization

reveals that KB-600 support has a more oxidized surface compared to its nitrogen-modified counterpart KB-600-N (Figure S12, Supporting Information), suggesting possible degradation due to surface oxidation processes. The nitrogen-doped carbon support, KB-600-N, exhibits greater resistance to electrochemical degradation compared to the pristine material of the same brand. This makes KB-600-N more resistant to corrosion-induced morphological changes and highlights its potential as a substrate for catalysts in PEMFC cathodes, where durability under harsh operating conditions is critical.

To investigate the functional characteristics of the electrocatalysts, they are tested in a three-electrode cell using a rotating disk electrode, see Figure S14 (Supporting Information). The voltammograms of all samples show characteristic hydrogen adsorption/desorption peaks in the low potential region (0–0.4 V vs RHE), and the highest currents are observed for Pt/KB-600-N in this region compared to other catalysts (Figure S14a, Supporting Information). The higher current in the double-layer region for the Pt/C catalyst compared to the commercial catalyst is attributed to its higher surface area of the support (Figure S14a,b, Supporting Information). Additionally, we present linear sweep voltammetry (LSV) results for all samples at different rotation rates in Figure S15 (Supporting Information).

The LSV profiles demonstrate the occurrence of ORR on the investigated catalysts. The more active Pt/KB-600-N sample shows a shift toward higher potential values (Figure S14c,d,

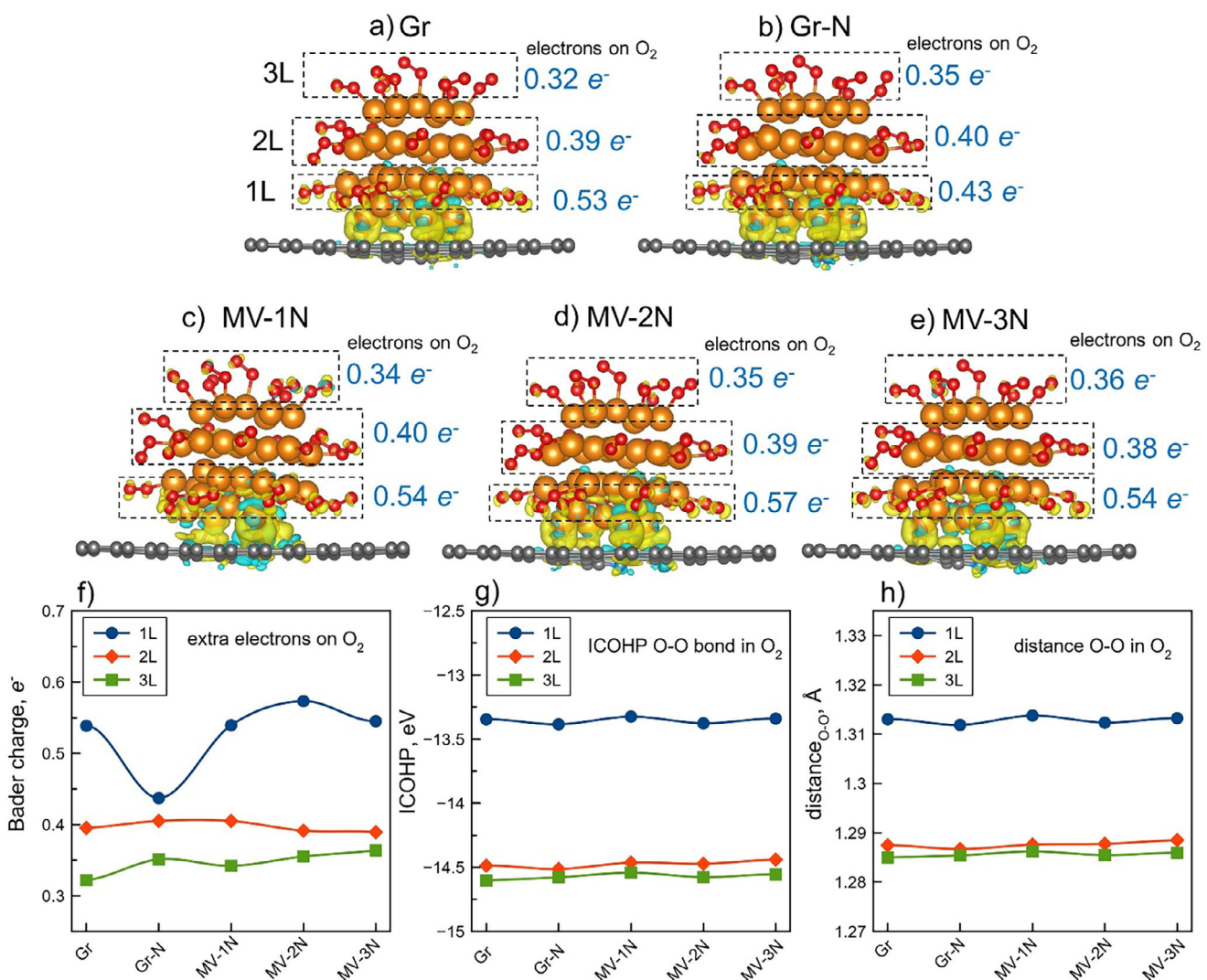


Figure 7. Atomic structures of Pt_{38} nanoparticle with adsorbed O_2 molecules located on the a) defectless graphene (Gr) and graphene with defects such as b) Gr-N (graphitic-N) and c-e) MV-1N/2N/3N (pyridinic-N) together with charge redistribution between graphene and Pt_{38} (isosurface value is $0.015 \text{ e } \text{\AA}^{-3}$) and the computed Bader's charges in average electrons per O_2 molecule for the first, second, third layers of O_2 . f) Average Bader's charge per O_2 molecule, g) ICOHP of O–O bond and h) O–O distances for the first, second, third layers of O_2 depending on defect types.

Supporting Information). The specific current density normalized to ECSA is calculated and presented in Table S5 (Supporting Information). Specific activity reflects the intrinsic catalytic activity of individual Pt sites. Mass activity (I_{mass}) depends on both I_{sp} and ECSA. Despite having high ECSA values, our samples exhibit superior specific activity compared to commercial reference catalysts, demonstrating more efficient platinum utilization. The performance of our catalyst is benchmarked against previous studies utilizing N-doped supports. A comprehensive comparison is provided in Table S6 (Supporting Information). The obtained Pt/KB-600-N material demonstrates superior mass activity (I_{mass}) and specific activity (I_{sp}) compared to other N-doped support-based catalysts reported previously. The high mass activity of the Pt/KB-600-N catalyst may be attributed to the co-existence of Pt nanoparticles and atomic Pt clusters on the support surface, as suggested

in reports.^[55] In our view, this synergistic effect requires further investigation for a conclusive interpretation.

The “Start-stop” protocol is selected for accelerated stress testing (AST), which aims to degrade the catalyst as a whole and simulates the operation of the catalyst at the cathode of a PEMFC during device start-up/shut-down cycles. This protocol has been developed by researchers at Toyota.^[56] A key feature of this protocol is testing in an oxygen atmosphere to simulate corrosive conditions at the PEMFC cathode. Figure 9 shows the CVs, LSVs, and histograms of changes in ESA and mass activity (I_{mass}) before and after AST for Pt/KB-600, Pt/KB-600-N, and commercial catalyst (COM). After AST, there is a significant decrease in current in the hydrogen region for all samples. However, for Pt/KB-600, this decrease is the most significant at 35%. This indicates degradation of the catalytic layer (Figure 9a–c). Meanwhile, the Pt/KB-600-N

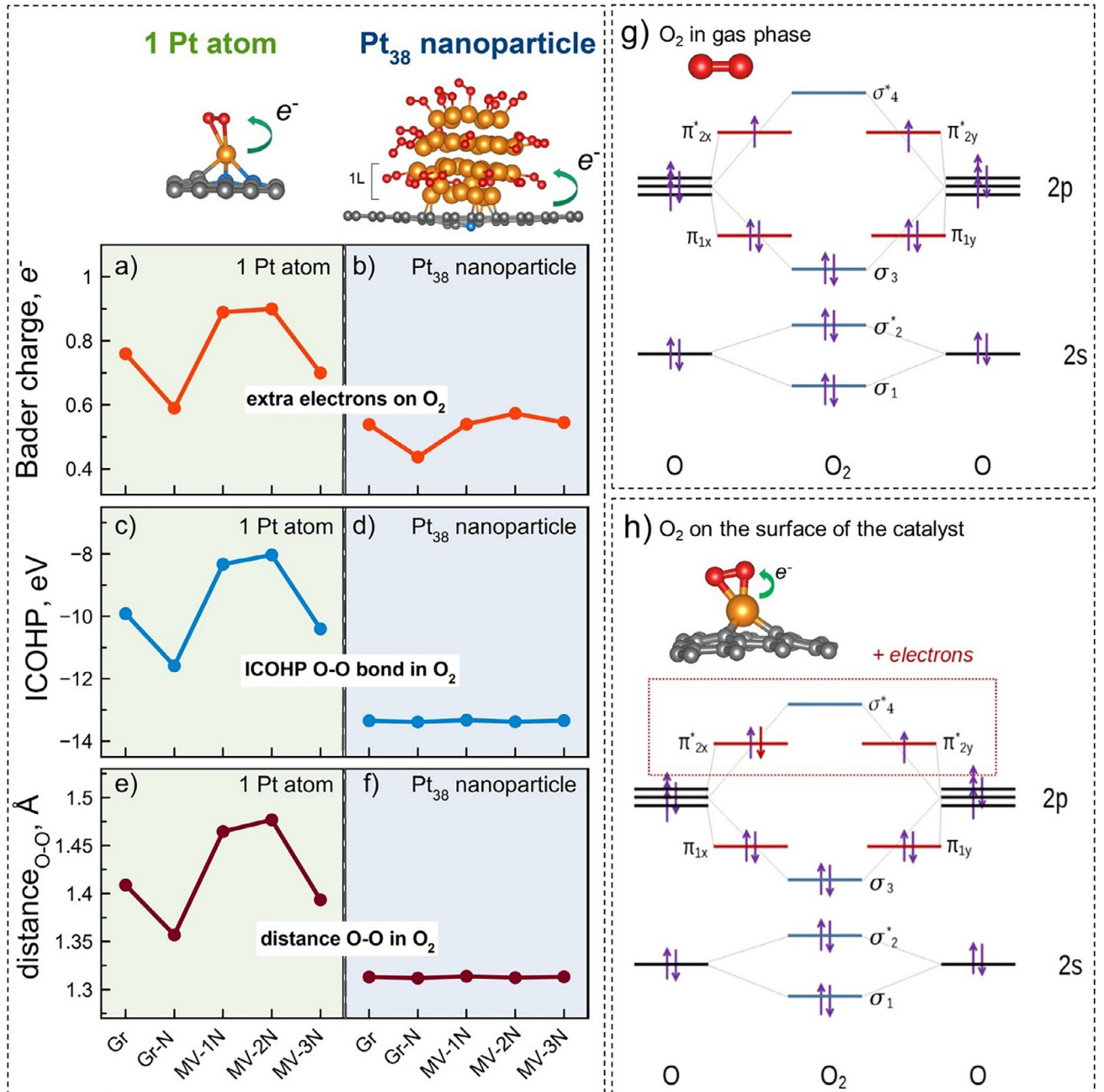


Figure 8. a,b) Computed Bader's charge on the O₂ molecule, c,d) ICOHP of O–O bond, and e,f) O–O distances in O₂ for a single Pt atom and the first platinum layer (1L) of Pt₃₈ nanoparticle depending on graphene defects. Schematic diagram of molecular orbitals for oxygen in g) gas phase and h) absorbed on the catalyst. When a catalyst donates electrons, it localizes the antibonding orbitals of an oxygen molecule, leading to the weakening of the O–O bond.

sample exhibits the lowest degree of degradation in terms of ESA (Figure 9g–i).

After AST, a shift in the half-wave potential ($E_{1/2}$) toward lower potentials is observed on the LSVs, indicating a significant loss of catalytic activity due to catalyst degradation (Figure 9d–f). The degradation resistance of Pt/KB-600-N and COM catalysts is similar; however, it is important to note that the focus should be not only on the degree of degradation but also on the residual per-

formance metrics. The initial and residual I_{mass} values for Pt/KB-600-N are approximately twice as high as those of the commercial reference sample.

Among the key processes leading to the degradation of electrocatalytic performance, the most commonly highlighted are dissolution and redeposition of platinum atoms, agglomeration and detachment of nanoparticles due to oxidation of the carbon support. Based on a comprehensive study of the electrochemical

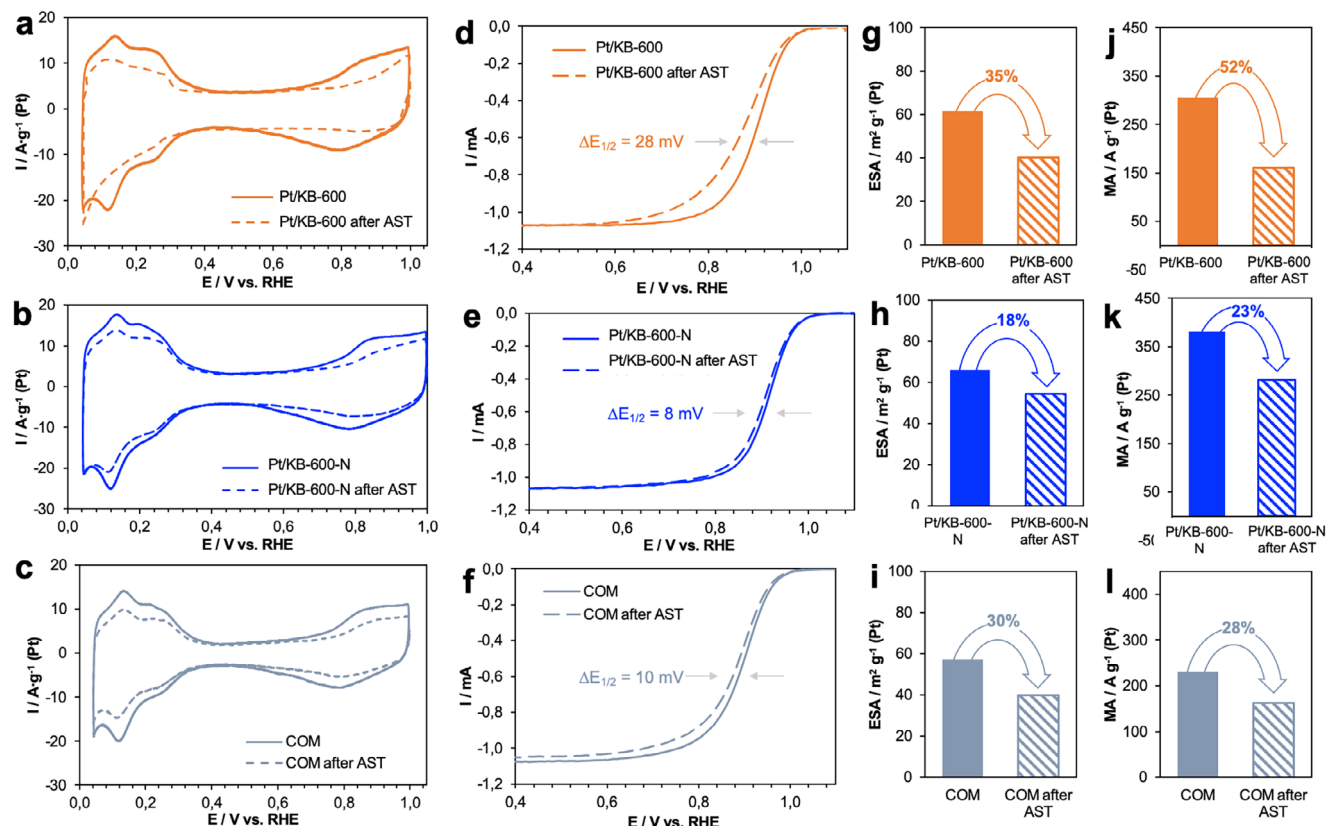


Figure 9. Cyclic voltammograms before (solid line) and after (dotted line) the AST for the a) Pt/KB-600, b) Pt/KB-600-N, and for c) COM materials. HClO_4 electrolyte saturated with Ar, 20 mV s^{-1} . Linear sweep voltammograms of the ORR before (solid line) and after (dotted line) the AST for the Pt/KB-600 (d), Pt/KB-600-N (e), and for the COM (f) materials. HClO_4 electrolyte saturated with O_2 , 20 mV s^{-1} . The RDE rotation speed is 1600 rpm. Histograms of changes in the ESA (g–i) and I_{mass} (j–k) values for the corresponding catalysts before and after the AST.

behavior of samples, we observe much higher stability in catalysts synthesized using N-doped supports compared to both initial support-based samples and commercial reference catalysts. To gain deeper insight into the underlying phenomena, we conducted a post-mortem microstructural analysis of the catalyst following the AST. For this purpose, the catalyst powder was carefully retrieved from the RDE after testing. Figure S16 (Supporting Information) depicts the catalyst's microstructure after degradation. A growth in the mean nanoparticle size to 3.4 nm is observed, primarily due to an increased fraction of particles in the $3.5\text{--}4.5 \text{ nm}$ range. The emergence of isolated nanoparticles larger than 5 nm was also noted. Concurrently, the population of $2\text{--}3 \text{ nm}$ nanoparticles decreased, which is consistent with the partial dissolution of surface platinum atoms followed by redeposition (Ostwald ripening) via a dissolution/redeposition mechanism (Figure S16d, Supporting Information). Importantly, the presence of platinum atoms and clusters is still identified in the post-AST HAADF STEM images (Figure S16c, Supporting Information).

Besides, we measure the current–voltage characteristics of the MEA using Pt/KB-600-N as the cathode catalyst (Figure S17, Supporting Information). The flow rates of hydrogen and oxygen are maintained at 220 and 680 mL min^{-1} , respectively. Both the cell and gas lines are kept at 80°C with 100% relative humidity for both gases, while the backpressure is maintained at 1.5 bar relative

to atmospheric pressure. The maximum power density of the MEA is 600 mW cm^{-2} (Figure S16a, Supporting Information). The obtained results are competitive with the state-of-the-art reported in refs. [57–61]. We believe that the application of this material with a modified support requires further optimization of the catalyst ink formulation (e.g., ionomer-to-carbon ratio, solvent) and the catalytic layer fabrication conditions. We will continue work in this direction to perform comparative testing after optimizing the catalyst ink composition.

3. Conclusion

In conclusion, we investigate how nitrogen modification of Ketjenblack EC-600JD carbon support improves the structure, morphology, and electrochemical properties of high-loading ($\approx 40 \text{ wt.\% Pt}$) electrocatalysts. We use the swift technique of doping with melamine to successfully incorporate nitrogen into the carbon support, which was confirmed by X-ray photoelectron spectroscopy and Raman spectroscopy. The formed nitrogen defects in the carbon supports act as traps for platinum atoms, improving the performance of the catalyst by preventing the agglomeration of platinum nanoparticles. A comprehensive density functional study revealed that pyridinic-N sites act as energetically favorable anchoring points for Pt nanoparticles, with binding energies $20\text{--}30\%$ higher than those on pristine

carbon. This theoretical insight explains our experimental observations of highly dispersed platinum nanoparticles of 2.5–3 nm in size and atomic clusters through HAADF-STEM. The obtained Pt/KB-600-N catalyst demonstrates exceptional performance. Its mass activity doubles that of commercial benchmarks, and it has remarkable stability, retaining 85% of its initial activity after accelerated stress tests. The pyridinic-N defects not only serve as an “anchor” for Pt nanoparticles but also promote charge transfer to adsorbed O₂, weakening O–O bonds. These two mechanisms—geometric stabilization and electronic modulation—together enhance both the longevity of the catalyst and its ORR activity. MEA testing confirmed the performance of the catalyst under real PEMFC conditions. At 80 °C and 1.5 bar, Pt/KB-600-N shows a maximum power density of 600 mW cm⁻² and low charge transfer resistance at the cathode.

Our results show that nitrogen doping of carbon is an effective strategy to improve the performance of electrocatalysts. Further steps must be taken to optimize the composition of the catalytic layer and fabrication parameters for the MEA.

4. Experimental Section

Materials and Reagents: Carbon black Ketjen Black EC600JD, hexachloroplatinic acid solution H₂PtCl₆·6H₂O (Aurat, TU 2612-034-00205067-2003), ethylene glycol (GOST 19710-27019), sodium hydroxide (analytic grade, 98%, Komponent-Reaktiv, GOST 4328-77), formalin (top grade, 37.5%, Aquatest, GOST 1625-2016), isopropanol (chemically pure, TU COMP 2-017-06), bidistilled water (electrical conductivity <5 µS cm⁻¹, GOST 58144-2018), hydrochloric acid HClO₄ (chemically pure, 66%, Vekton, TU 6-09-2878-8-84), isopropanol (extra-pure grade, 11-5 OP-1 TU 2632-064-44493179-01), 1% Nafion solution (Dupont), gaseous argon (99.998%, Research Institute of Construction Materials, TU 6-21-12-94), melamine, deionized water, HiSPEC4000 (Pt/C, 40% platinum loading, Johnson Matthey).

Preparation of the Nitrogen-Doped Carbon Support: Ketjenblack EC600JD with a surface area of 1370 m² g⁻¹, mixed with melamine, was subjected to heat treatment in a tube furnace under an argon atmosphere at 600 °C for 1 h. The initial support was hereinafter referred to as KB-600, and the N-doped one based on it was referred to as KB-600-N.

Method to Synthesize the Catalyst: Pt nanoparticles supported on KB-600-N were obtained via the chemical reduction of platinum from the solution of hexachloroplatinic acid by formaldehyde in the aqueous organic suspension containing the carbon support (Figure S1, Supporting Information). The solution was heated to 80 °C and kept under constant stirring for 3 h. After natural cooling, H₂SO₄ was added drop by drop (for deposition of platinum NPs on the carbon support), and the suspension was stirred for 1 h. The resulting material was separated by filtration with repeated rinsing with bidistilled water and isopropanol. The sample was dried at 70 °C in a vacuum furnace until a constant weight was achieved. The resulting sample was hereinafter referred to as Pt/KB-600-N. For comparison, Pt supported on commercial carbon support (KetjenBlack EC600JD) was prepared using the same method and labeled as Pt/KB-600. Additional information on the materials and synthesis stages can be found in the Supporting Information. The well-known commercial product – HiSPEC4000 (COM) – was selected as the reference sample.

Characterization of Materials: The composition and structure of the synthesized catalysts were characterized using a combination of advanced analytical techniques. The metal mass fraction was determined by gravimetry, heating the samples to 800 °C in a UED-7-10D muffle furnace. XRD analysis was performed on a Bruker D2 PHASER diffractometer using Cu K α radiation ($\lambda = 1.5406 \text{ \AA}$) with measurements taken in the 2 θ range of 15° to 55° and a step size of 0.04°. The textural properties of the catalysts were evaluated using nitrogen adsorption isotherms at 77 K, measured with an Autosorb-6B analyzer (Quantachrome Instruments, USA).

Samples were prepared by heating in dynamic vacuum to 350 °C until a residual pressure of <5 × 10⁻² Torr was achieved. Raman spectroscopy was performed using a Renishaw inVia Reflex spectrometer with a 514 nm laser, recording spectra in the range of 50–3500 cm⁻¹. XPS measurements were conducted using a SPECS PHOIBOS-150 spectrometer with Al K α radiation; the charge correction was applied by setting the C1s peak at 284.4 eV.

High-resolution transmission electron microscopy (TEM) and high-angle annular dark-field scanning TEM (HAADF-STEM) were conducted using a Thermo Fisher Scientific Themis Z microscope (resolution: 0.7 nm) for Pt/KB-600 and Pt/KB-600-N and a JEOL JEM-F200 microscope (resolution: 0.2 nm) for COM. Nanoparticle size distributions were determined by analyzing at least 300 particles from TEM images, while energy-dispersive EDX was performed using a Bruker Xflash 6T/60 Quantax 400-STEM system.

Electrochemical characterization included the electrochemically active surface area (ESA) and ORR activity using cyclic voltammetry (CV) and LSV. AST was performed to evaluate catalyst stability, with degradation assessed by changes in ESA and mass activity. For all electrochemical measurements, including those for the commercial HiSPEC4000 (COM) catalyst, identical procedures for ink preparation, electrode coating, electrolyte (0.1 M HClO₄), and testing conditions (temperature, gas flow, etc.) were strictly maintained to ensure a fair and direct comparison. The current–voltage characteristics were measured for the MEA utilizing Pt/KB-600-N as the cathode catalyst. Additional details on the materials and measurements can be found in the Supporting Information.

Supporting Information

Supporting Information is available from the Wiley Online Library or from the author.

Acknowledgements

This research was conducted within the framework of the Strategic Academic Leadership Program of the Southern Federal University (Priority 2030). The authors are grateful to the Shared Use Center “High-Resolution Transmission Electron Microscopy” (SFedu, Rostov-on-Don) for conducting the TEM studies and to the Shared Use Center “National Center of Investigation of Catalysts” (Boreskov Institute of Catalysis, Novosibirsk) for conducting the TEM, EDX, XPS, and BET studies. Density functional calculations were carried out using resources of the Center for Information and Computing of Novosibirsk State University and Zhores supercomputers at Skoltech. The authors also thank A. S. Konstantinov for conducting the Raman spectroscopy measurements and A. B. Ayupov for conducting the low-temperature N₂ adsorption measurements. The research conducted at the Southern Federal University was financially supported by the Russian Science Foundation (Grant No. 24-79-10162, <https://rscf.ru/project/24-79-10162/>).

Conflict of Interest

The authors declare no conflict of interest.

Data Availability Statement

The data that support the findings of this study are available from the corresponding author upon reasonable request.

Keywords

DFT, electrocatalysts, N-doped carbon supports, oxygen reduction reaction (ORR), platinum nanoparticles

Received: August 25, 2025

Revised: October 25, 2025

Published online:

- [1] R. Riassé, C. Lafforgue, F. Vandenberghe, F. Micoud, A. Morin, M. Arenz, J. Durst, M. Chatenet, *J. Power Sources* **2023**, *556*, 232491.
- [2] K. Ehelebe, N. Schmitt, G. Sievers, A. W. Jensen, A. Hrnjic, Y.-L. Zhang, L. Zhao, Z.-B. Wang, M. Ma, L.-X. Shen, J. Liu, B. Xu, Y.-L. Zhang, L. Zhao, Z.-B. Wang, Z.-B. Wang, *ACS Energy Lett.* **2022**, *7*, 816.
- [3] F. Guo, T.-J. Macdonald, A. J. Sobrido, L. Liu, J. Feng, G. He, *Adv. Sci.* **2023**, *10*, 21.
- [4] L. Huang, S. Zaman, X. Tian, Z. Wang, W. Fang, B. Y. Xia, *Acc. Chem. Res.* **2021**, *54*, 311.
- [5] M. Wang, J. Teng, S. Zaman, S. Zhang, X. Chen, K. Zhang, X. Wang, Z. Li, M. Wu, *Green Chem.* **2024**, *26*, 4432.
- [6] Y. Xu, B. Zhang, *Chem. Soc. Rev.* **2014**, *43*, 2439.
- [7] M. Ma, L.-X. Shen, J. Liu, B. Xu, Y.-L. Zhang, L. Zhao, Z.-B. Wang, *Rare Met.* **2024**, *43*, 4198.
- [8] X. Ren, Y. Wang, A. Liu, Z. Zhang, Q. Lv, B. Liu, *J. Mater. Chem. A* **2020**, *8*, 24284.
- [9] Y. Jiang, Y. Wang, J. Qian, Y. Mu, Z. Li, T. Zhao, L. Zeng, *Int. J. Hydrogen Energy* **2024**, *51*, 578.
- [10] Y. X. Xiao, J. Ying, H.-W. Liu, X.-Y. Yang, *Higher Education Press Limited Company* **2023**, *17*, 1677.
- [11] E. Antolini, *Appl. Catal., B* **2009**, *88*, 1.
- [12] A. L. Dicks, *J. Power Sources* **2006**, *156*, 128.
- [13] H. Inoue, K. Hosoya, N. Kannari, J.-I. Ozaki, *J. Power Sources* **2012**, *220*, 173.
- [14] N. Tachibana, Y. Yukawa, K. Morikawa, M. Kawaguchi, K. Shimano, *SN Appl. Sci.* **2021**, *3*, 338.
- [15] Y. Holade, C. Morais, K. Servat, T. W. Napporn, K. B. Kokoh, *Phys. Chem. Chem. Phys.* **2014**, *16*, 25609.
- [16] H. Daimon, S. Yamazaki, M. Asahi, T. Ioroi, M. Inaba, *ACS Catal.* **2022**, *12*, 8976.
- [17] Q. Xue, J. Huang, D. Yang, B. Li, C. Zhang, *RSC Adv.* **2021**, *11*, 19417.
- [18] H. Schmies, E. Hornberger, B. Anke, T. Jurzinsky, H. N. Nong, F. Dionigi, S. Kuhl, J. Drnec, M. Lerch, C. Cremers, P. Strasser, *2018*, *30*, 7287.
- [19] L. Nayak, M. Rahaman, R. Giri, in *Carbon-Containing Polymer Composites*, Springer, Cham, Switzerland, **2019**, p. 65.
- [20] M. R. Benzigar, S. N. Talapaneni, S. Joseph, K. Ramadass, G. Singh, J. Scaranto, U. Ravon, K. Al-Bahily, A. Vinu, *R. Soc. Chem. 2018*, *47*, 2680.
- [21] K. Ham, S. Chung, J. Lee, *J. Power Sources* **2020**, *450*, 227650.
- [22] E. A. Moguchikh, K. O. Paperzh, A. A. Alekseenko, E. N. Gribov, N. Y. Tabachkova, N. V. Maltseva, A. G. Tkachev, E. A. Neskoromnaya, A. V. Melezhik, V. V. Butova, O. I. Safronenko, V. E. Guterman, *J. Appl. Electrochem.* **2022**, *52*, 231.
- [23] I. N. Novomlinskiy, Q. Xue, J. Huang, D. Yang, B. Li, *Electrocatalysis* **2021**, *12*, 489.
- [24] C. S. Il, S. U. Lee, R. Choi, J. T. Park, S. W. Han, *ChemPlusChem* **2013**, *78*, 1252.
- [25] V. A. Golovin, N. V. Maltseva, E. N. Gribov, A. G. Okunev, *Int. J. Hydrogen Energy* **2017**, *42*, 11159.
- [26] B. Wu, H. Meng, D. M. Morales, F. Zeng, J. Zhu, B. Wang, M. Risch, Z. J. Xu, T. Petit, *Adv. Funct. Mater.* **2022**, *32*, 31.
- [27] X. Cai, et al., *ACS Appl. Energy Mater.* **2024**, *7*, 8705.
- [28] A. A. Trofimov, A. M. Leonova, N. M. Leonova, T. A. Gevel, *J. Electrochem. Soc.* **2022**, *169*, 020537.
- [29] E. Hornberger, et al., *ACS Appl. Mater. Interfaces* **2022**, *14*, 18420.
- [30] S. Stambula, N. Gauquelin, M. Bugnet, S. Gorantla, S. Turner, S. Sun, J. Liu, G. Zhang, X. Sun, G. A. Botton, *J. Phys. Chem. C* **2014**, *118*, 3890.
- [31] N. Tachibana, et al., *Carbon* **2017**, *115*, 515.
- [32] C. C. Hsu, et al., *Desalination* **2020**, *481*, 114362.
- [33] J. Li, et al., *RSC Adv.* **2022**, *12*, 12377.
- [34] S. J. ho, et al., *RSC Adv.* **2017**, *7*, 20738.
- [35] W. Shen, W. Fan, *J. Mater. Chem. A Mater.* **2013**, *1*, 999.
- [36] Y. Xia, R. Mokaya, *Adv. Mater.* **2004**, *16*, 1553.
- [37] S. Ott, et al., *Appl. Catal. B* **2022**, *306*, 121118.
- [38] S. Ott, F. Du, M. L. Luna, T. A. Dao, B. R. Cuanya, A. Orfanidi, P. Strasser, *Electrochem. Soc.* **2022**, *169*, 054520.
- [39] K. Morishige, T. Kawai, S. Kitakata, *J. Phys. Chem. C* **2014**, *118*, 4664.
- [40] Z. Zafar, et al., *Carbon* **2013**, *61*, 57.
- [41] Zhao., et al., *Science* **2011**, *333*, 999.
- [42] J. Kaufman, S. Metin, D. Saperstein, *Phys. Rev. B* **1989**, *39*, 13053.
- [43] L. G. Bulusheva, A. V. Okotrub, I. A. Kinloch, I. P. Asanov, A. G. Kurenya, A. G. Kudashov, X. Chen, H. Song, *Phys. Status Solidi B* **2008**, *245*, 1971.
- [44] N. Hellgren, et al., *Carbon* **2016**, *108*, 242.
- [45] D. J. Morgan, *C* **2021**, *7*, 51.
- [46] X. Yan, T. Xu, G. Chen, S. Yang, H. Liu, Q. Xue, *J. Phys. D: Appl. Phys.* **2004**, *37*, 907.
- [47] I. Bertóti, M. Mohai, K. László, *Carbon* **2015**, *84*, 185.
- [48] K. Paperzh, et al., *Carbon* **2024**, *16*, 100383.
- [49] G. Al-Sayed', J.-C. D. Oliveira, P. Pichat, *J. Photochem. Photobiol. A: Chem.* **1991**, *58*, 99.
- [50] F. M. Hassan, V. Chabot, J. Li, B. K. Kim, L. Ricardez-Sandoval, A. Yu, *J. Mater. Chem. A* **2013**, *1*, 2904.
- [51] Z. Tian, S. Dai, D. Jiang, *Chem. Mater. Am. Chem. Soc.* **2015**, *27*, 5775.
- [52] Sh. K. Shaikhutdinov, M. Schildnerberger, M. Noeske, G. Mestl, *React. Kinet. Catal. Lett.* **1999**, *67*, 129.
- [53] X.-F. Li, K.-Y. Lian, L. Liu, Y. Wu, Q. Qiu, J. Jiang, M. Deng, Y. Luo, *Sci. Rep.* **2016**, *6*, 23495.
- [54] Y. Zhang, Y. Kang, X. Wei, C. Chen, Y. Zhai, C. Zhu, L. Jiao, X. Lu, Y. Yamauchi, *ACS Nano* **2025**, *19*, 24013.
- [55] J. Liu, et al., *Nature* **2017**, *8*, 15938.
- [56] T. Nagai, C. Jahn, H. Jia, *Electrochem. Soc.* **2019**, *166*, F3111.
- [57] J. A. Prithi, N. Rajalakshmi, G. Ranga Rao, *Int. J. Hydrogen Energy* **2018**, *43*, 4716.
- [58] L. Wang, et al., *Energy* **2020**, *261*, 114277.
- [59] J. Wang, Z. Huang, W. Liu, C. Chang, H. Tang, Z. Li, W. Chen, C. Jia, T. Yao, S. Wei, Y. Wu, Y. Li, *Am. Chem. Soc.* **2017**, *139*, 17281.
- [60] L. Huang, Y.-Q. Su, R. Qi, D. Dang, Y. Qin, S. Xi, S. Zamani, B. You, S. Ding, B. Y. Xia, *Angew. Chem. Int. Ed.* **2021**, *60*, 25530.
- [61] Y. Hu, M. Zhu, X. Luo, G. Wu, T. Chao, Y. Qu, F. Zhou, R. Sun, X. Han, H. Li, B. Jiang, Y. Wu, X. Hong, *Angew. Chem. Int. Ed.* **2021**, *60*, 6533.